Tectonophysics 843 (2022) 229591

Contents lists available at ScienceDirect

Tectonophysics

journal homepage: www.elsevier.com/locate/tecto

The 2020 Samos Mw7 earthquake: Source model depicting complexity and rupture directivity

V. Plicka [a,*], F. Gallovič [a], J. Zahradník [a], A. Serpetsidaki [c], E. Sokos [c], N. Vavlas [b], A. Kiratzi [b]

[a] Charles University, Faculty of Mathematics and Physics, Czech Republic
[b] Aristotle University of Thessaloniki, Department of Geophysics, Greece
[c] University of Patras, Department of Geology, Seismological Laboratory, Greece

ARTICLE INFO

Keywords:
Samos
Aegean
Rupture directivity
Earthquake
Slip model
Transtension

ABSTRACT

The October 30, 2020, Mw7 Samos earthquake ruptured a north-dipping offshore normal fault, bounding the Samos basin; it accommodated ~N-S extension and can be viewed as a modern manifestation of the basin evolution. It caused 118 fatalities, generated a tsunami, and caused a co-seismic uplift of 20 to 35 cm of the NW part of Samos Island. Using broadband, strong-motion, and geodetic data, we constrain the location and source geometry of the mainshock. A multiple-point source model suggests three sequential subevents providing 20 s of source duration. Our finite-fault kinematic model confirms the prevalence of large slip amplitudes (~2.4 m) along the entire ruptured area and the up-dip and westward rupture propagation. This directivity is independently confirmed by Apparent Source Time Functions inferred from regional recordings using a herein developed new variant of the empirical Green's function method. Static GNSS displacements from inland stations yield a near-surface co-seismic slip of ~1 m amplitude, contributing to any interpretation of the observed island uplift. The 2020 Samos event showed that in the spatially heterogeneous oblique transtentional regions in the back-arc Aegean region, normal faults bounding the basins are capable to rupture in M7 earthquakes, provoke tsunami generation, and constitute a constant threat to the nearby coastal areas of both Greece and Turkey.

1. Introduction

The focus of our study is a normal faulting event: the October 30, 2020 Samos earthquake of moment magnitude Mw7.0 (GCMT, Dziewonski et al., 1981; Ekström et al., 2012). It occurred ~9 km offshore the northern coast of Samos Island in the eastern Aegean Sea (Fig. 1). Kinematically, the broad tectonic setting (Fig. 1 inset) is governed by: i) the rapid (~24 mm/y) westwards escape of the Anatolia block towards the Aegean (Weiss et al., 2020), facilitated by the operation of the dextral strike-slip North Anatolian Fault (NAF), in conjunction with the sinistral strike-slip East Anatolian Fault (EAF) and ii) the even faster (~35 mm/yr) southward retreat of the trench and of the Hellenic subduction zone, which is rolling back towards Africa (Jolivet et al., 2015; Faccenna et al., 2014). In this context, shearing deformation, imposed from the westward Anatolia escape, interacts with extensional deformation, related to slab rollback, that is why the deformation is often described as transtensional (Brun et al., 2016). As the trench retreats southwards, it pulls the overriding Aegean plate, causing significant north-south extension and thinning of the overlying lithosphere (Karabulut et al., 2019; Le Pichon et al., 2019). The extension is so intense that the Aegean Sea and the surrounding lands rank among the most rapidly extending continental regions worldwide (Meng et al., 2021), resulting in a frequent occurrence of normal faulting earthquakes, as the one studied here.

The northern coastline of Samos island (Fig. 1) is bounded by dominant E–W striking normal faults, mainly inferred from sea topography. Soon after the occurrence of the mainshock, the causative fault was inferred (Ganas et al., 2020) and associated with the Samos Basin Fault from bathymetry surveys (Nomikou et al., 2021). The fault was included in the fault databases as Kaystrios Fault (Caputo and Pavlides, 2013) or as North Samos Fault (Chatzipetros et al., 2013). The mainshock predominantly ruptured the western segment of this fault, with no documented historical event (since ~1700). Contrarily, several strong events (e.g., in 1873 and 1893, M ~ 6.5) may be associated with its eastern segment (Kiratzi et al., 2021, and references therein).

The specific focus of our work is to search for any source complexity, and assess the characteristics of the rupture history to provide a finite-fault kinematic model of the mainshock. Because many models are

* Corresponding author.
E-mail address: vp@karel.troja.mff.cuni.cz (V. Plicka).

https://doi.org/10.1016/j.tecto.2022.229591
Received 24 May 2022; Received in revised form 19 August 2022; Accepted 27 September 2022
Available online 1 October 2022

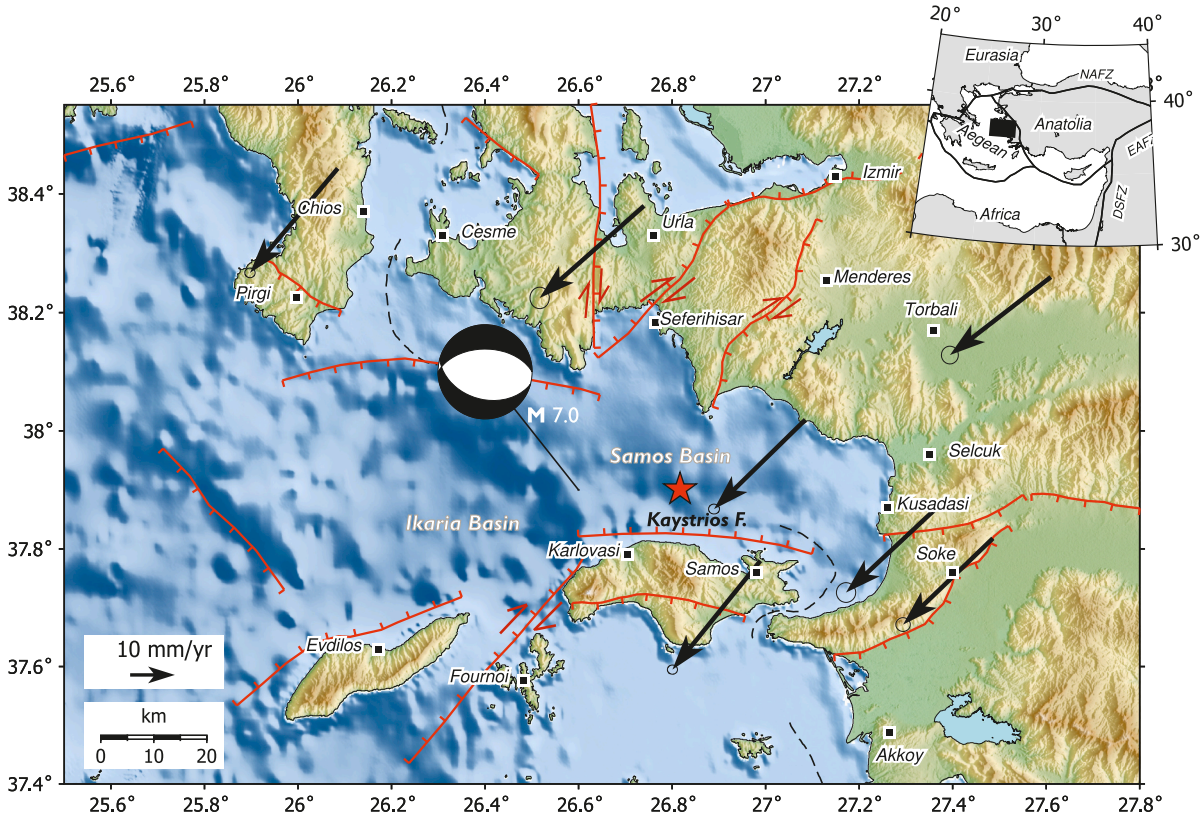

Fig. 1. Epicenter location (star) and centroid moment tensor solution (beach-ball) of the Samos 2020 M7 earthquake, alongside active faults (red lines; from Caputo and Pavlides, 2013) and GPS-derived long-term horizontal velocity vectors (black arrows; data from England et al., 2016). The study area within the broader tectonic context is shown in the inset (NAFZ: North Anatolian Fault Zone; EAFZ: East Anatolian Fault Zone; DSFZ: Dead Sea Fault Zone). (For interpretation of the references to colour in this figure legend, the reader is referred to the web version of this article.)

already available, our work is structured as follows: we first discuss the so far available findings and the similarities and differences among them, then we present the motivation and the scope of our work, and finally discuss the Samos event within the regional tectonic context.

1.1. Key characteristics of the sequence and open issues

Life loss, environmental effects, observed tsunami: The Samos earthquake caused 2 fatalities and 19 minor injuries at Samos Island, but 116 deaths and over 1030 injuries in Izmir (Turkey), a city of ~4 M inhabitants (Cetin et al., 2020). The damage in the Izmir Bay area (Bayrakli district), ~70 km away from the epicenter, was mainly attributed to site amplification of ground shaking, at site frequencies in the range of 0.7 to 1.6 Hz, for both stiff and soft soil sites (Makra et al., 2021). The mainshock caused a moderate tsunami, which affected nearby Samos Island and cities along the Aegean coast of Turkey, resulting in substantial property losses. The maximum tsunami inundation (i.e., max horizontal intrusion) was 2.31 m, and its maximum runup was 3.82 m (Dogan et al., 2021). The tsunami arrived within ~10 min to the coast of NW Samos Island and within 20 min to the coast of Turkey, and sea recession was the leading motion (Triantafyllou et al., 2021). No consensus has been reached on the tsunami triggering mechanism, whether it was generated by co-seismic seafloor displacement, earthquake-induced submarine landslides along the fault scarp, or a combination of both. Field reconnaissance measured co-seismic shorelines' uplift of 20 ± 5 to 35 ± 5 cm at the western coastline of northern Samos (Evelpidou et al., 2021). GPS-derived displacements indicated tectonic uplift of almost 10 cm on Samos Island (Ganas et al., 2021). A key issue contributing to the discussion regarding the observed uplift and tsunami generation is to constrain whether the rupture reached the seafloor. These are key parameters to get an idea of the capability of normal faulting earthquakes to generate tsunamis.

Hypocenter location of the mainshock and vertical distribution of the aftershocks: In the aftermath of the mainshock, initial relocations were available, based on published P- and S-wave arrivals at stations located in Greece and Turkey (Papadimitriou et al., 2020; Foumelis et al., 2021). Subsequently, many groups provided relocated aftershock catalogs (Karakostas et al., 2021; Kiratzi et al., 2021; Lentas et al., 2021). The main difference between the results is the depth of the mainshock and the depth extent of the sequence. Karakostas et al. (2021) calculated the mainshock depth at 16.88 km and the aftershocks at depths mainly between 10 and 15 km. Whereas the other two groups (Kiratzi et al., 2021; Lentas et al., 2021) converge on shallower depth for the mainshock (8 to 10 km) and predominant spread of the aftershocks at shallow depths, in the range of 5 to 10 km, in agreement with the results of our work.

Identification of the fault plane - dip angle variability: The nearly *E*-W striking, the north-dipping nodal plane has been inferred as the fault plane, based on geodetic data (Ganas et al., 2020) and seismic data (Papadimitriou et al., 2020; Karakostas et al., 2021; Taymaz et al., 2022; Kiratzi et al., 2021; Zúñiga and Tan, 2021 and references therein). Notably, for other normal faulting events in the eastern Aegean Sea, for example, the 2017 Kos-Bodrum Mw6.6 earthquake in the Gulf of Gökova, resolving the direction of fault dip was not straightforward from the available data (Kiratzi and Koskosidi, 2018; Konca et al., 2019 and references therein). On the contrary, the value of the dip angle was rather variable (see Table 2). It ranged from the dip as low as 29° (USGS), and 37° (GCMT) to as steep as 55° (KOERI). Normal faults with dip angles smaller than ~40° are not common within the overriding Aegean plate, even though reflection profiles show otherwise (Laigle et al., 2000), warranting careful analysis.

Source complexity, slip distribution models, inferred westward rupture

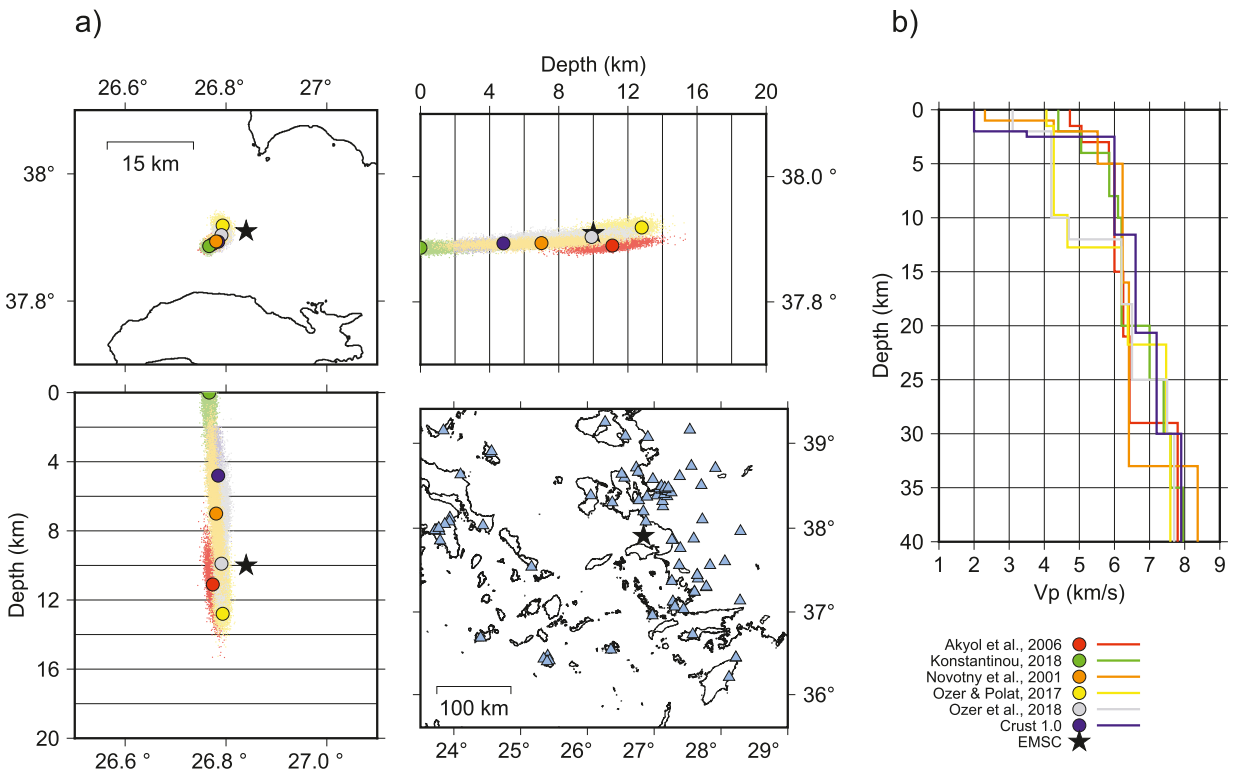

Fig. 2. Relocation of mainshock hypocenter: a) Best-fit NonLinLoc solutions (circles) and their uncertainties (colored cloud-dots) obtained from the inversion of P- and S- phase arrivals at the stations (shown by grey triangles). The black star is the EMSC location. The panels correspond to map and side views. b) The different velocity models explored. The Crust1.0 model (Laske et al., 2013) is sampled at latitude = 37.5°N and longitude = 26.5°E. All models provide a stable epicenter position ±1.0 km and shallow (<12 km) depth. Inverting P-phases only gives comparable results.

propagation: Even though finite-fault slip models have already been published, a systematic search for source complexity and the presence of any subevents has not been performed. Complexity can only be inferred from the number and location of slip patches (asperities). The comparative characteristics of the, so far, published slip models depend on the inversion scheme, data, fault model parameterization, accuracy of the Green's functions, and the frequency band used, among other parameters. Based mainly on teleseismic data and only two strong motion components, the model by Karakostas et al. (2021) shows a small peak slip amplitude (~1 m) and a deeply rooted slip patch (at ~25 km), which differs from other models based on similar data (Chousianitis and Konca, 2021). The model by Kiratzi et al. (2021), based on regional seismic data in the frequency band between 0.02 and 0.08 Hz, indicates: a) slip confined in an area 32 km × 15 km, and at very shallow depths less than ~10 km; b) peak slip amplitude of ~3.5 m, situated ~18 km to the west of the hypocenter, c) top of the fault at 0.5 km, nearly reaching the seafloor and d) a dominant up-dip and westward rupture propagation. The kinematic rupture inversion of Lentas et al. (2021) is based on local strong motion data, adopting fault geometry, slip direction, and seismic moment from the GCMT solution without further optimization. Their results suggest a non-uniform bilateral rupture on a ~ 60 km × ~20 km fault, with the main rupture propagating towards the west, with a maximum slip of ~2.5 m. Chousianitis and Konca (2021) jointly inverted geodetic (static GPS offsets and high-rate waveforms), teleseismic, and strong-motion data, filtered between 0.02 and 0.4 Hz. Their preferred model is dominated by a slip patch 30 km × 10 km, along strike and dip, respectively. Taymaz et al. (2022) using back-projection and kinematic and dynamic finite-fault modeling of seismic data, obtained a rupture of 50 km × 20 km with two main asperities and a maximum slip of 3.2 m. Ren et al. (2022) considered a segmented fault with two asperities of up to 3 m of slip, reaching shallow depths to explain the observed tsunami waveforms from three tidal gauges.

To sum up, the so-far published models are quite variable, specifically regarding the peak slip amplitude and the spatial distribution of the slip patches along strike and depth. These issues are crucial to interpreting the damage pattern and providing valuable input to the modelers if the observed tsunami could relate to sufficient seafloor dislocation.

1.2. Scope of the present work

To alleviate the variability of the published results we reanalyze the earthquake using a dataset consisting of broadband (BB) and strong motion (SM) digital recordings and GNSS static displacements. Our workflow is as follows:

a) relocation of the mainshock hypocenter and of the aftershock cloud to reassess the spatial and vertical distribution of the sequence, benchmarking the consistency of available velocity models;
b) multiple-point source modeling to assess the fault geometry, especially the dip angle of the fault plane, and search for source complexity in variable frequency bands;
c) finite–fault kinematic slip inversion including optimization of the fault geometry and slip direction to constrain the spatial and vertical distribution of the slip, including its peak amplitude and how close to the seafloor the rupture propagated;
d) inference of the rupture directivity by inspection of the finite-extent source slip model and apparent source time functions (ASTF) retrieved by a new Empirical Green's Function (EGF) method, originally developed herein. Worth noting that no previous similar ASTF-EGF analysis has been performed in the so far publications about the Samos earthquake.
e) synthesis of the results within the regional seismotectonic context.

Table 1
Mainshock hypocenter parameters as obtained from P- and S-wave arrivals benchmarking different velocity models within NonLinLoc code. 'Depth' is the formal, best-fitting value. For uncertainty, see Fig. 2 and the axis size of the confidence ellipsoid (a1 = semi-major, a2 = semi-minor, a3 = semi-moderate). The semi-major axis is oriented almost vertically. The location provided by EMSC is listed for comparison.

Velocity Model	Origin Time	Latitude °N	Latitude °N	Depth (km)	Confidence Ellipsoid Axis (km)		
					a1	a2	a3
Akyol et al., 2006	11:51:25.10	37.8899	26.7738	11.1	2.2	0.8	0.9
Konstantinou, 2018	11:51:24.28	37.8864	26.7667	0.0	2.7	0.8	1.0
Novotný et al., 2001	11:51:25.15	37.8938	26.7805	7.0	4.4	0.9	1.0
Özer and Polat, 2017	11:51:24.51	37.9188	26.7933	12.8	2.3	1.0	1.4
Özer et al., 2018	11:51:23.64	37.9037	26.7911	9.9	4.1	1.1	1.1
Crust1.0 (Laske et al., 2013)	11:51:24.71	37.8934	26.7845	4.8	2.7	0.9	0.9
EMSC	11:51:25.70	37.91	26.84	10.0			

2. Hypocenter locations and basic parameters

2.1. Mainshock hypocenter location

We manually picked P- and S-wave arrivals from strong-motion (SM) and broadband (BB) stations, 81 in total, at epicentral distances from 20 to 290 km (Fig. S1). Several 1-D velocity models (VM) applicable to the region are available, which allowed us to benchmark their efficacy to provide consistent results regarding the mainshock hypocenter and get an estimate of the uncertainties. We examined 8 velocity models and located the mainshock using the probabilistic NonLinLoc code of Lomax et al., 2000 (see Section 1A, and Figs. S1, S2 in the Supplement for details). The location of the epicenter is very stable, at 37.900°N and 26.817°E (±1 km) within all the models tested (Fig. 2 and Table 1). Although the depth is generally the most challenging parameter to constrain (with error for each velocity model of up to 4 km), all models indicate hypocenter depths in the upper crust, at ~12 km and shallower. The models of Konstantinou (2018) and Novotný et al. (2001) provide comparable P- and S- residuals ~ ± 1 s at all epicentral distances (Fig. S2). The model of Novotný et al. (2001), derived from surface-waves dispersion, has proven to be very efficient in describing wave propagation in the Aegean area, especially at low frequencies used in the finite-fault modeling.

2.2. Relocation of aftershocks

The manually picked events recorded during the first 40 days, initially located with Hypoinverse (Supplement B), were relocated with HypoDD (Waldhauser and Ellsworth, 2000; Waldhauser, 2001). Among all the velocity models examined regarding their location uncertainties and their hypocenter distribution (see Section 1B and Figs. S3 to S6 in the Supplement for details), the model of Özer et al. (2018) was adopted as the most appropriate. This model was derived from the most recent seismic experiment in the study area and provided the best travel-time data fit and better hypocenter distributions without artificial linear depth concentrations.

Fig. 3 summarizes the final relocated dataset of ~1300 events in total. The aftershock's spatial distribution indicates that the area just west of the hypocenter is depleted in aftershock productivity compared to the nearby eastern region (see also Figs. S6 in the Supplement). This observation is the first proxy for the inferred locus of the major slip, later confirmed by our slip model. The aftershocks tend to distribute in four clusters. The cross-sections (Fig. 3 top panels) depict that: i) the sequence evolved in the upper crust (h < 15 km) and the aftershocks are mostly up-dip from the hypocenter ii) the causative fault dips to the north, and iii) secondary structures were activated. The main cluster comprising the mainshock's hypocenter borders the Samos northern coastline, and all aftershock mechanisms associated with it depict pure normal faulting along *E*-W striking planes (Karakostas et al., 2021). The cluster formed west of the main one (cross-section C1C2, Fig. 3) can be considered the westernmost part of the main causative fault, dipping slightly steeper than the main one to the NNE and indicating normal faulting as well. The westernmost cluster (cross-section B1B2, Fig. 3) represents a NE-SW alignment following the Ikaria basin topography (Nomikou et al., 2021). The easternmost cluster (cross-section A1A2, Fig. 3), inland Samos Island, shows a fault dipping steeply, almost vertically. These secondary structures can be associated with focal mechanisms that exhibit dextral strike-slip motions (Karakostas et al., 2021, Fig. 3). The aftershocks distribution suggests that strike-slip faults border the main activity area.

3. Multiple point source (MPS) modeling of the mainshock

Before finite-fault modeling, we investigate the source process of the mainshock using the multiple-point source modeling tool available in the ISOLA software package (Zahradník and Sokos, 2018; Liu and Zahradník, 2020, and references therein). We describe the rupture process as a sequence of points of moment release episodes, known as subevents. This is an approximate representation of the continuous source process. It depends on epicentral distances and frequency range, visualizing the same source either as a point at low frequencies or a series of points at higher frequencies. We adopt the velocity structure of Novotný et al. (2001) to calculate full-waveform synthetics.

We started with the employment of waveforms from BB stations, in the epicentral distance range of 263 to 456 km, to perform a centroid moment tensor (CMT) inversion, in the frequency range between F*min* = 0.005 Hz and F*max* varied as 0.02, 0.03, and 0.04 Hz. The minimum and maximum frequencies are constrained by noise (natural and instrumental) and the accuracy of the velocity model, respectively. For the lowest F*max* value, we found a poor spatial resolution of centroid and a slightly overestimated moment magnitude (Mw = 7.04, compared to Mw = 7 of GCMT). For the other values of F*max* we obtained Mw =7.0 and 6.9, respectively, with satisfactory waveform fit (variance reduction VR = 0.8 and 0.6), and a consistent position of the centroid, shifted 20-km westward of the epicenter, and with the centroid time ~ 10 s relative to origin time. The latter can be taken as a proxy of the source half-duration, as later confirmed by more detailed modeling. The optimal centroid depth was between 6 and 8 km, representing an improvement compared to the artificially fixed 12 km depth of GCMT. Besides, we found the centroid depth almost independent of the used velocity model, being significantly more stable than the hypocenter depth. Regarding the focal mechanism, we found a stable, high-percentage double-couple deviatoric source (DC > 85%), with strike/dip/rake (s/d/r) angles equal to 270°/50°/−100°, slip vector azimuth/plunge = 15°/49°, which is close to the GCMT solution (Table 2), as shown in Fig. 4.

Subsequently, by employing waveforms from SM stations in the distance range of 30 to 155 km and the frequency range from 0.04 to 0.09 Hz, the earthquake appears as a multiple point source. To stabilize the inversion, we kept the depth fixed at 6 km and searched for the best-fitting positions of point sources along an *E*-W striking horizontal line. Using the double-couple constrained inversion, we identified three relatively stable subevents, shown in Fig. 4, alongside our subsequently discussed slip model. The subevents' focal mechanisms denote predominant normal faulting. A cumulative tensor sum of the subevents'

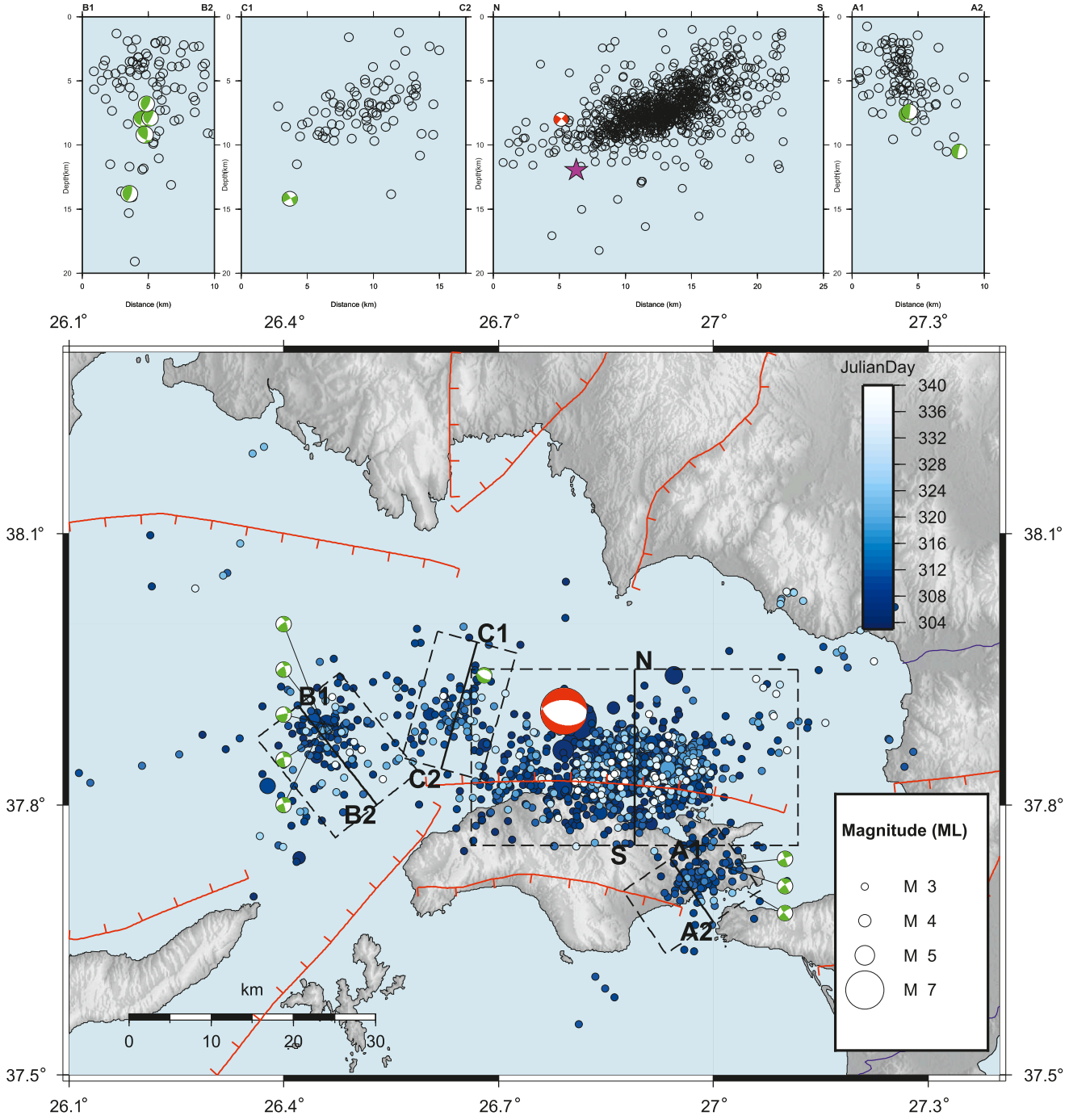

Fig. 3. Spatial distribution of relocated aftershocks of the period October 30 to December 4, 2020, and designated cross-sections (top panels). The red beach ball represents the moment tensor solution of the mainshock, herein calculated, while green beach balls denote selected aftershock moment tensors from Karakostas et al. (2021). (For interpretation of the references to colour in this figure legend, the reader is referred to the web version of this article.)

MTs yields an effective point-source mechanism with s/d/r equal to 246°/44°/−125°, slip vector azimuth/plunge = 20°/35°, being close to the GCMT solution (Kagan angle 21°), Mw = 7.0 and VR = 0.63. Considering also a possible fourth subevent, we found it unstable, providing only negligible improvement to the waveform fit (Fig. S7). For example, our models with one, two, or three subevents featured VR ~ 0.33, 0.57, 0.63, while the fourth subevent increased VR just to 0.67. Therefore, we finally adopt the 3-point model. We intentionally do not go into more specific details; changing any parameter, e.g., F*max*, or removing any single station, the results are obviously changing but the gross features of the MPS model remain stable, as follows.

The first subevent is situated ~4 km east of the epicenter, indicating an initial eastward rupture propagation. The other two subevents, located at ~12 and ~ 32 km west of the epicenter, support the predominant westward propagation, further confirmed by our modeling. The focal mechanisms of the subevents (Fig. 4), expressed with s/d/r, have as follows: *sub1* 271°/46°/−106°, *sub2* 225°/40°/−155°, *sub3* 249°/54°/−110°. The subevents occur at ~6, ~10, and ~ 15 s after origin time (OT), providing ~20 s of the total source duration. This agrees with the source time function inferred by Geoscope, using the SCARDEC method (Vallée et al., 2011). Using the subevents' source mechanisms and the non-negative-least squares (NNLS) method of

Table 2
Moment tensor solution for the mainshock calculated here alongside published ones (the letter f next to the depth value, H, denotes that it was fixed during the inversion).

Centroid Time	Centroid location		H (k	Mo (Nm)	M_w	Nodal Plane 1 (Fault Plane)			Nodal Plane 2			slip vector (NP1)	Reference
hh:mm:ss	Lat°N	Lon°E	m)	×e19		strike°	dip°	rake°	strike°	dip°	rake°	az°/plunge°	
11:51:37	37.90	26.59	8	3.95	7.0	270	50	−100	79	38	−115	15/49	This study
11:51:44	37.80	26.70	12f	4.09	7.0	275	29	−87	93	60	−91	2/29	USGS
11:51:26	37.90	26.80	14	3.76	7.0	260	36	−116	111	58	−72	21/32	IPGP
11:51:34	37.80	26.70	12f	4.01	7.0	270	37	−95	96	53	−86	6/37	GCMT
11:51:26	37.80	26.80	11	3.90	7.0	289	40	−69	82	53	−107	352/37	INGV
11:51:26	37.90	26.80	10	–	7.2	275	45	−96	103	45	−85	13/45	OCA
11:51:24	37.90	26.80	11	3.26	6.9	270	46	−91	95	43	−87	1/46	AFAD
11:51:27	37.90	26.80	15	3.50	7.0	272	48	−93	97	41	−85	6/48	GFZ
11:51:26	37.90	26.80	13	2.81	6.9	270	50	−81	76	41	−101	346/49	UOA
11:51:24	37.90	26.81	6	2.65	6.9	294	54	−65	76	43	−120	346/47	NOA
11:51:27	37.90	26.80	10	3.00	6.9	272	55	−93	97	34	−85	7/55	KOERI

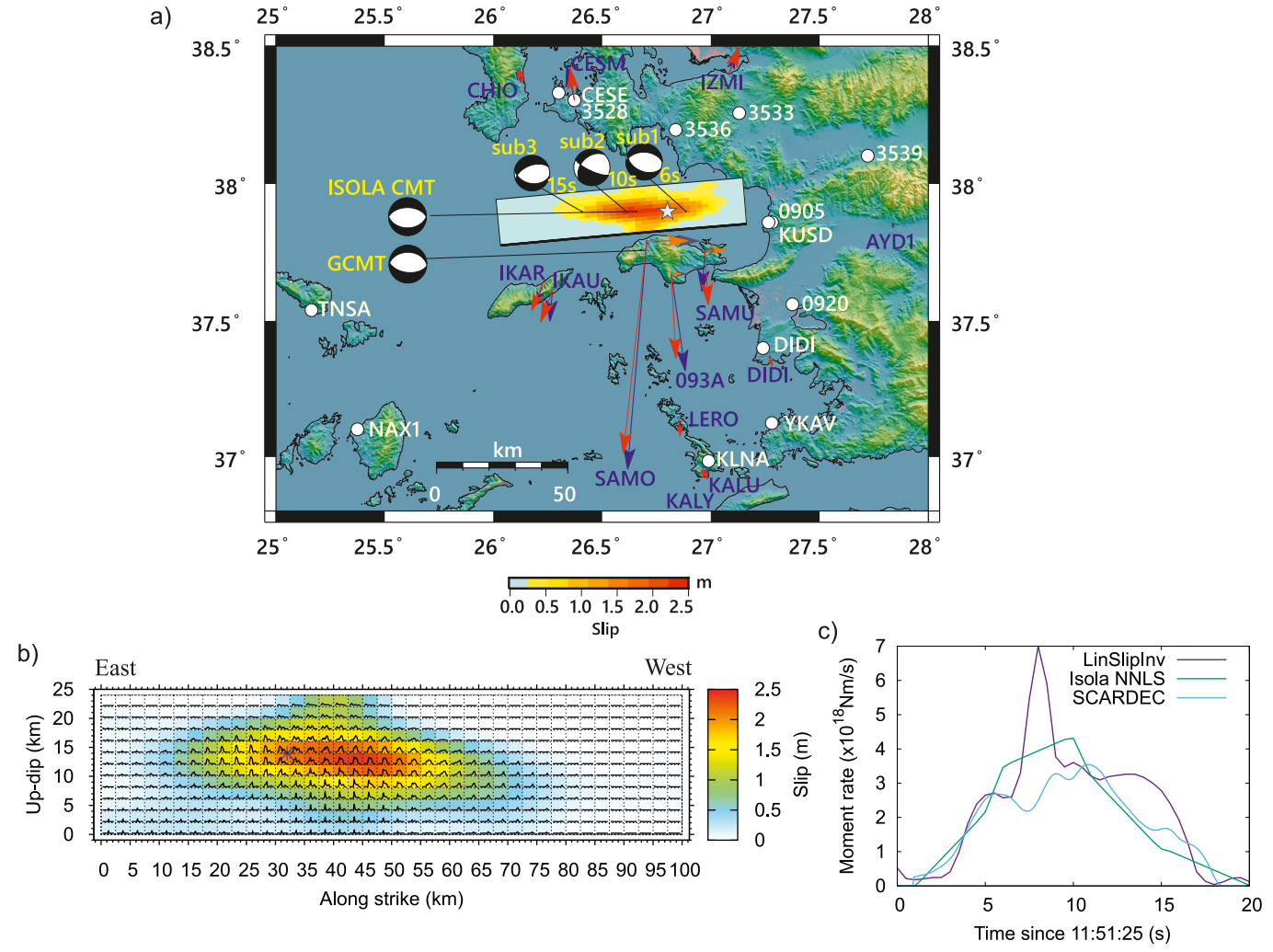

Fig. 4. a) Map view of slip distribution (colour-coded) from the LinSlipInv kinematic slip inversion on north-dipping fault (rectangle). Star is the preferred epicenter. Circles show strong motion stations used in the inversion. Arrows show GNSS daily solutions (blue) and the respective synthetic displacements (red); vertical (upward) motions on SAMOS island are formally plotted as eastward arrows for clarity (observed in grey, synthetic in orange). Maximum horizontal displacement 35.7 cm was measured at the SAMO station. Multiple-point source model (sub 1,2,3) is shown by small beach balls, with depicted timing after the origin time. Isola CMT and GCMT solutions are shown for reference. b) Cross section of slip model shown in a) with slip rate functions superimposed (maximum scaled to 0.5 m/s). c) Moment rate functions from LinSlipInv, Isola NNLS and SCARDEC database (Vallée and Douet, 2016), depicting the source duration of ~20 s. (For interpretation of the references to colour in this figure legend, the reader is referred to the web version of this article.)

Lawson and Hanson (1974), we calculated the moment rate function (MRF); for the technique, see appendix of Zahradník and Sokos (2014). This MRF is compared to the one obtained from the slip inversion model (Fig. 4). Both functions depict a total source duration of ~20 s. The agreement with teleseismic studies of GCMT and SCARDEC guarantees that our analysis of regional data is not biased.

Table 3
Geometry of the fault considered in the finite-fault inversion and main characteristics of the inferred rupture model.

Parameter	Value
Seismic Moment	4e19Nm (constrained from GCMT)
Moment magnitude, M (Mw)	7.0 (constrained from GCMT)
Fault length × width	100 km × 24 km
Strike/dip/rake of the fault (dips to N)	265°/40°/−110°
Fault center coordinates	37.899°N, 26.589°E
Fault top depth	0 km
Fault bottom depth	13 km
Rupture propagation	Unconstrained
Average displacement along the ruptured area	1.2 m
Maximum displacement	2.4 m
Ruptured area (slip >0.2 m)	60 km × 20 km

4. Finite-Fault kinematic rupture model

We used the Linear Slip Inversion (LinSlipInv) method of Gallovič et al. (2015) to infer kinematic finite-fault description of the rupture process, a technique applied to many previous earthquakes in Greece (Sokos et al., 2015, 2016, 2020). Table 3 lists the quantities describing the setting of the calculation. In LSI, slip rate functions, spanning the entire rupture duration, are discretized in time and space. Synthetic Green's functions are calculated by the discrete wavenumber method adopting the Novotný et al. (2001) crustal model (as in ISOLA analysis) in a frequency range of 0.02 to 0.15 Hz. At higher frequencies, the details of the source and wave propagation in the medium (e.g., effects due to local heterogeneities) could not be adequately captured by the 1D velocity model. The data are displacement waveforms acquired from local strong motion stations (Fig. 4) filtered in the same way as the Green's functions, using the 4th order causal (single-pass) Butterworth filter. We also employ static GNSS data adopted from Ganas et al. (2021).

We stabilize the inverse problem by i) assuming prior covariance function with k^{-2} decay at large wavenumbers k, ii) prescribing seismic moment inferred by the CMT inversion using ISOLA modules, and iii) positivity of the slip rates. Regarding the latter, we use the NNLS approach of Lawson and Hanson (1974). We point out that the source description in the LSI method is very general, with no prior constraints on the position of the nucleation point, rupture speed, and shape of slip-rate functions. A drawback of this loose parameterization is that the result is sensitive to artifacts and biases imposed by the imperfect station distribution and smoothing (Gallovič and Zahradník, 2011; Zahradník and Gallovič, 2010). To this end, the result must be carefully interpreted considering lessons learned from previous synthetic tests and real-data applications (Gallovič, 2016; Gallovič et al., 2015).

The fault is modeled as a rectangle, 100 km × 24 km along strike and dip, respectively. We grid-searched its position and mechanism: strike

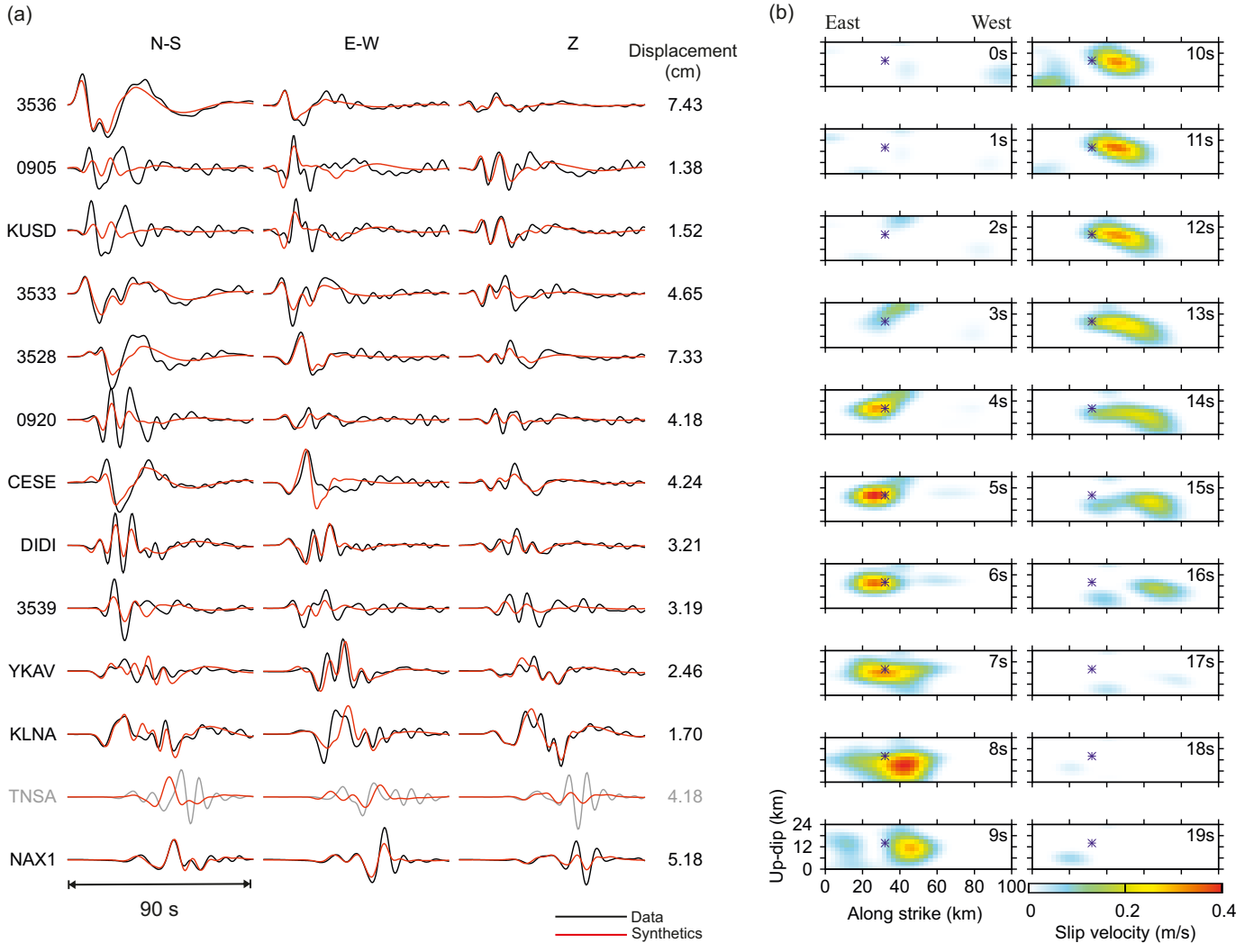

Fig. 5. a) Waveform fit of displacement recordings in a frequency range of 0.02–0.15 Hz. The waveform in grey (TNSA) was not used in the inversion. b) Slip rate snapshots of our preferred rupture model inferred by the LinSlipInv kinematic inversion method (Fig. 4).

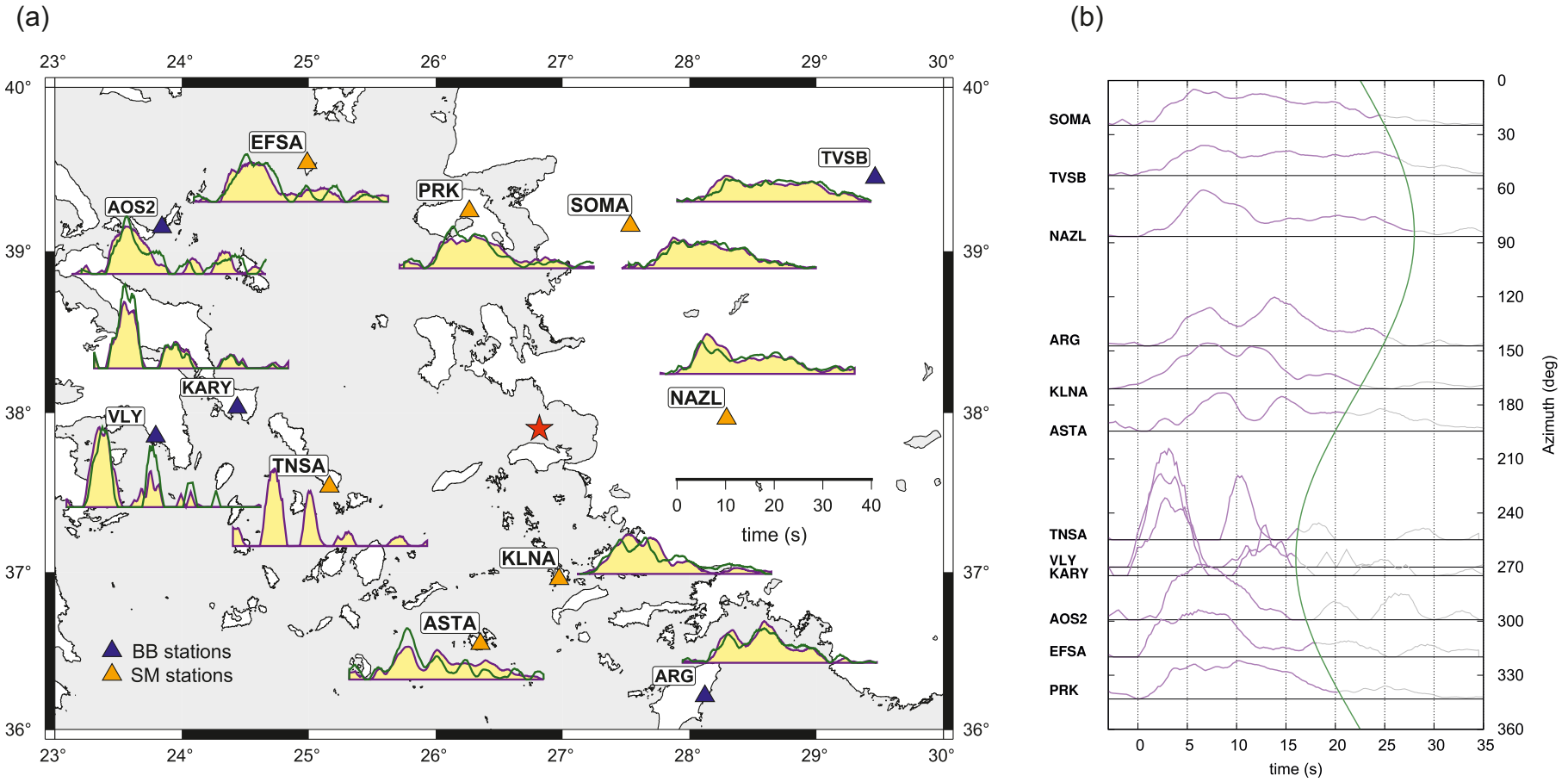

Fig. 6. Apparent source time functions (ASTFs) obtained from the EGF method at regional broadband (blue triangles) and strong motion (orange triangles) stations in a) a map view and b) as a function of azimuth (for simplicity, event used as EGF1 is drawn). The red star denotes the epicenter. Magenta and green ASTFs in panel a) are obtained from EGF1 and EGF2, respectively. Station TNSA has data just for EGF1. Narrow and high amplitudes of ASTFs confirm the westward rupture propagation at western stations (KARY, VLY, TNSA) in contrast to longer duration and smaller amplitudes at the rest of the stations. The green curve line depicts the theoretical variation of the apparent duration for the rupture azimuth of 265°, total rupture duration of 22 s, and 7 s long westward-directive rupture propagation. (For interpretation of the references to colour in this figure legend, the reader is referred to the web version of this article.)

(240°, 250°, 260°, 265°, 270°), dip (35°, 40°, 45°), and rake (−100°, −110°, −120°, −130°), position in the north-south direction was varied by ±5 km with respect to the centroid. The best waveform fit (waveform variance reduction VR = 0.618 and GNSS VR = 0.978, see Fig. 5) and the least artifacts occurrence were attained for the initial fault position (with its center fixed in the centroid) and for strike/dip/rake = 265°/40°/−110°.

The preferred slip model (Fig. 4) shows that the main slip episode occurred west of the epicenter. The slip is located both at depth, but also close to the surface. We point out that the shallow slip is illuminated almost exclusively by the GNSS data. Indeed, if the GNSS data are neglected in the inversion, the surface slip is not revealed, while the closest GNSS is underestimated by about 50% (see Fig. S8). Noting that the waveform improves only slightly when GNSS data are omitted (VR = 0.623), the seismic data proves insensitive to the temporal evolution of the shallow slip, at least in our frequency range and with our station coverage. For comparison, we added also the SCARDEC STF into Fig. 4. The duration is comparable, the slip inversion has a more pronounced peak at 8 s, related to the onset of the unilateral westward rupture propagation.

Snapshots of the inferred slip rates (Fig. 5) suggest that the rupture started close to the epicenter (not a priori prescribed in the inversion). On the dipping fault, the hypocenter lies at a 6 km depth. The rupture propagates bilaterally mainly up-dip for the initial ~3 to 4 s (see the analogy with the first subevent of the MPS (Multiple point source) inversion delayed by 6 s after the origin in Fig. 4a, and the slip-rate peaks at 4 to 8 s in the LSI snapshots of Fig. 5b). After that, the rupture continues to the west, i.e., towards mainland Greece, creating the major slip within 8 to 16 s after the origin time, extending ~40 km westwards of the hypocenter and up to shallow depths (see the second and third subevent in the MPS model and the dominant slip patches in the EGF and LSI models).

The area that ruptured extends 60 km along strike and 20 km along dip. The peak slip reaches 2.4 m. It is thus similar to Lentas et al. (2021), who used the same inversion method but without optimizing the fault geometry and slip direction and employing only the seismic data. The other published models are characterized by smaller rupture areas (and thus larger peak slip), which might be related to the strength of the smoothing constraint in the individual applications. Indeed, comparing slip distribution inferred by the kinematic (Pizzi et al., 2017) and dynamic (Gallovič et al., 2019) rupture inversions for the 2016 Amatrice earthquake, the latter resulted in ~1/3 times smaller rupture length. Since the Amatrice application utilized stations at shorter distances than in the Samos earthquake, the true rupture extent of Samos might be between 30 and 40 km. A similar estimate would be obtained, if the rupture area is defined assuming a contour of ~0.5 to 0.8 m of minimum slip.

As mentioned above, the shallow slip is constrained just by the GNSS data with almost no effect on the waveform fit (Fig. S8). Therefore, we consider the temporal evolution of the surface rupture as poorly constrained. We hypothesize that the rupture had a relatively long slip rate duration at shallow depths due to long rise times and/or slow rupture propagation, with small slip-rate peaks and thus weak radiation of seismic waves, especially at periods dominating the displacement waveforms (~10 to 20 s).

For our kinematic model parameterization, the rupture speed can be only roughly estimated, keeping in mind that only a very smoothed image has been revealed (Gallovič et al., 2015). For the dominant westward faulting, the speed can be estimated from the slip-rate peak position at 45 km along strike at 8 s and the termination of the rupture 8 s later occurring at about 70 km (see the snapshots in Fig. 5). This suggests a relatively high rupture speed of about 3 km/s. Obviously, we cannot rule out the possibility that the rupture could have propagated slower/faster or more episodically during each moment release episode.

5. Apparent Source Time Functions (ASTFs)

Rupture directivity is a key element of the physics of earthquakes, and here we seek to explore this feature employing the empirical Green's functions (EGF) approach. Several methods were developed to obtain ASTF (e.g., Hartzell, 1978; Mueller, 1985; Mori and Hartzell, 1990; Bertero et al., 1997; Courboulex et al., 1997; McGuire, 2004; Vallée, 2004; Roumelioti et al., 2009; López-Comino and Cesca, 2018). Most of them are based on spectral deconvolution, requiring careful stabilization. Here we suggest a simple new alternative technique based on the NNLS technique, fully operating in the time domain, assuming that the ASTF is implicitly positive and seismic moment is constant across the stations (see supporting Section 4 and Figs. S9-S13).

We calculate apparent source time functions (ASTFs) from regional waveform data by the NNLS technique and investigate their duration and amplitude variation with azimuth. This method only requires finding an aftershock to serve as an empirical EGF, originating at a similar depth and location as the mainshock and having a similar focal mechanism. No further assumptions are made (no source or velocity model is needed). The aftershock sequence was depleted in strong aftershocks, specifically in the suitable magnitude range M5 to M6. This significantly narrowed the number of suitable EGFs. Exploiting the available data, we finally selected two aftershocks (EGF1, M5 of October 31, 2020, 05:31 UTC, and EGF2, M5.1 of October 30, 2020, 15:14). The waveform similarity supports the similar focal mechanisms of the selected EGFs (Cetin et al., 2020) and the mainshock. For these two events, we obtain two ASTFs. The ASTFs are searched in a time interval from −5 s to 35 s relative to origin time, i.e., in the 40 s time window. We invert the full seismogram at each station, including P and S waves and all three components. We have also calculated ASTFs using the P or S waves groups only, but the results were similar to the inversion of complete records. The frequency band of inversion was chosen at 0.05 to 0.5 Hz, but higher frequencies can also be used. We have inverted the original acceleration, velocity, or integrated records, and the results were stable.

ASTFs obtained from events 1 and 2 are very similar at all stations (Fig. 6a). Such similarity indicates the inversion stability and good selection of both events as an EGF. The inferred ASTFs (Fig. 6) from stations located orthogonal to the fault strike (EFSA, PRK, SOMA, TVSB in the north, and KLNA, ASTA, ARG in the south) depict longer pulse duration and lower amplitudes, compared to those located along strike (KARY, VLY, TNSA in Greece and NAZL in Turkey), supporting westward rupture propagation. More specifically, NAZL lies in the backward direction of rupture propagation, whereas KARY, VLY, and TNSA are in the forward direction, exhibiting narrow, high-amplitude pulses.

Assuming a horizontal rupture propagation featuring a unilateral rupture propagation on a part of the fault, apparent duration $\tau(f)$ as a function of station azimuth f can be described by

$$\tau(f) = T_1 + T_2\left(1 - \frac{V_r}{V_{P,S}}cos(f-\alpha)\right) = T_D - \frac{L_2}{V_{P,S}}cos(f-\alpha) \quad (1)$$

Here $T_D = T_1 + T_2$ is the total rupture duration, T_1 is the rupture duration corresponding to the nondirective part of the fault, and $T_2 = L_2/V_R$ is the rupture duration of the fault portion L_2 with assumed unilateral rupture propagation at the speed V_R. The $V_{P,S}$ is the velocity of P or S waves, and α is the rupture directivity azimuth.

We have tested several combinations of T_D and $\frac{L_2}{V_{P,S}}$ to find the optimum ones that provide the best match with the observed duration of the ASTFs (Fig. 6b). The direction of rupture α = N265 ° is fixed, obtained from our fault slip model. The best fit to the data is for values: T_D= 22 s ± 2 s, $\frac{L_2}{V_{P,S}} = 7\ s$ (curve in Fig. 6b). If we consider the S-wave velocity in the source depth (e. g., V_s = 3.5 km/s in the Novotný et al. (2001) model), the length of the directive zone is L_2 = 24.5 km, which corresponds to the estimate from the kinematic finite-fault modeling. We note

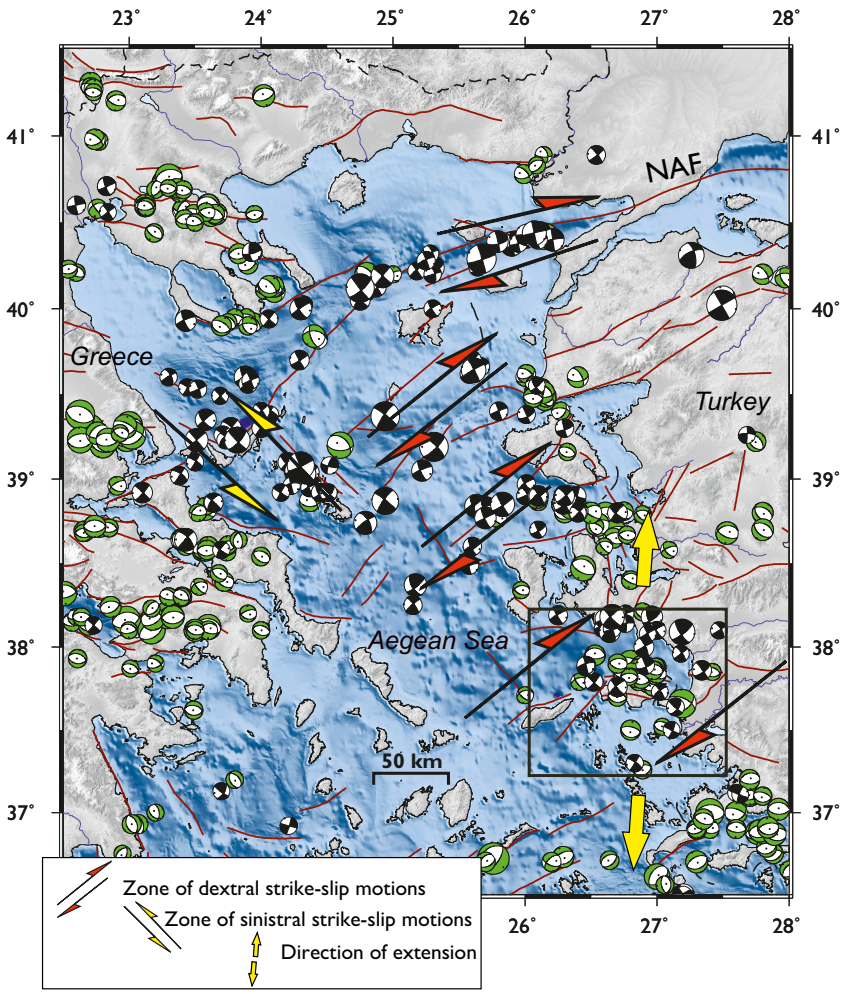

Fig. 7. Shear motions within the Aegean Sea, as depicted by earthquake focal mechanisms, M ≥4.0, 1964 to 2021 (beachballs: green = normal faulting; black = strike-slip faulting;. Dextral motions are imposed from the North Anatolian Fault as it splays into *en-echelon* NE-SW dextral strike-slip faults and associated grabens (pull-apart structures) in the Aegean Sea, terminating close to the eastern Greek coastline, along an NW-SE trending zone of sinistral strike-slip motions. (NAF: North Anatolian Fault). Note the diminish of shear motions south of ~37.5°N parallel. The rectangle encloses the area analyzed in Fig. 8, while the divergent arrows above and below the rectangle denote the direction of extension. (For interpretation of the references to colour in this figure legend, the reader is referred to the web version of this article.)

that the rupture velocity V_R cannot be inferred from the durations of the ASTFs (Eq. 1).

6. Discussion

6.1. Samos earthquake - main results

Our study of the Samos earthquake complements the other published results described in Sec. 1.1, using different inversion techniques (e.g., MPS and LinSlipInv). Variability of the methods and data employed has the potential to show a possible weakness of the inversions. In the case of Samos, probably due to its relatively smooth simple dominantly unilateral rupture, most published results are similar.

Our relocation confirms hypocenter depth in the range of 6 to 12 km (not deeper). With a missing local seismic network, and the reading of noisy S waves picks at some stations, we can not get more precise depth information. We constrain the epicenter with an uncertainty of ±1 km, using six existing velocity models. Our relocated aftershocks suggest that the sequence deployed at shallow depths (h < 15 km) in the brittle upper crust.

Although we do not prescribe the hypocenter a priori, the resulting space-time history of slip points to nucleation at a depth of 6 km, further narrowing the depth uncertainty. We optimized the fault geometry and slip direction during our kinematic finite–fault slip inversion. The best strike/dip/rake values are 265°/40°/−110°, corresponding to an *E*-W striking normal fault, moderately (40°) dipping to the north, with a predominantly normal slip component.

Multiple point source modeling, finite-fault kinematic slip inversion, and analysis of Apparent Source Time Functions (ASTFs) suggest the following rupture evolution scenario. The rupture initially propagated eastward or bilaterally during the first ~7 s to at least 5 km east of the epicenter. Then the rupture propagated unilaterally to the west for at least 30 km of the epicenter for another ~10 s. Globally, the along-strike directivity of normal faults has been so far relatively rarely reported (Calderoni et al., 2015; Pacor et al., 2016). This event thus contributed to the database of such faults in the Eastern Mediterranean. Additionally, our slip model indicates a 1.1 m slip reaching the sea bottom, offshore the Karlovasi town. The temporal resolution of this shallow slip patch is poor due to the insensitivity of the seismic waveforms, suggesting rather long rise times and/or slow rupture propagation at the shallow depths. Nevertheless, this inference is consistent with Ren et al. (2022) who inferred a similar shallow slip patch at approximately the same position to model the observed small tsunami on Samos Island. Nevertheless, we admit that our subfaults are 2.5 × 2 km large and thus 1.1 m at the shallowest subfaults does not necessarily imply surface (seabottom) slip. Moreover, the smoothing constraint has the potential to artificially enlarge the rupture area. However, we do not dispose of any additional data.

6.2. The Samos earthquake within the broader tectonic context

The Samos earthquake is a clear manifestation of basin opening, that is of the Samos basin, due to N-S (back-arc) crustal stretching on the overriding Aegean plate. The extension of the Aegean crust was initially very localized, but since the middle Miocene, it became distributed along the entire Aegean domain, facilitating the widespread formation

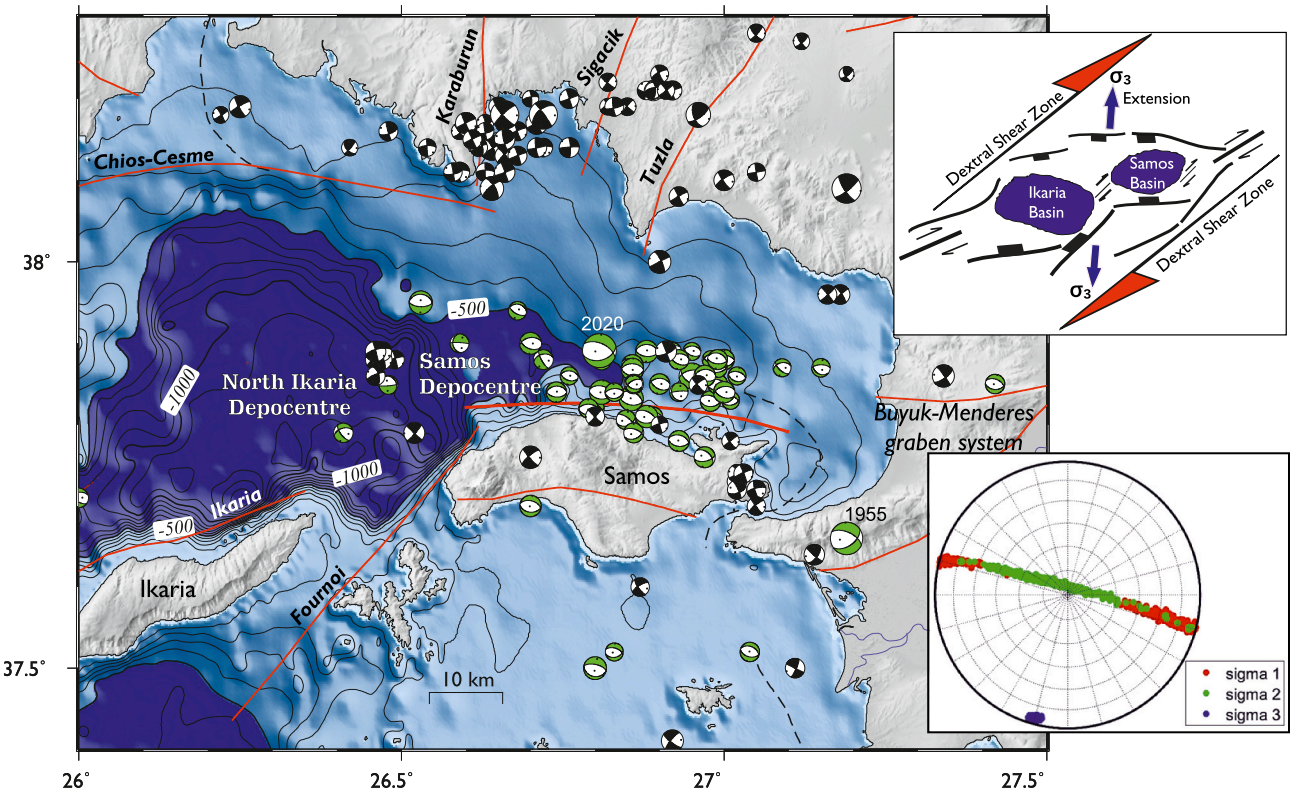

Fig. 8. Close-up of our study area to show how the Samos event nicely fits the regional transtensional tectonics, with the evolution of two depocentres: the North Ikaria Depocentre and the Samos Depocentre. The former is a wide asymmetric deep (~1400 m) depression, while the latter is a smaller and considerably shallower (~690 m) depression. The focal mechanisms (beach-balls) show prevalence of ~E-W trending normal faulting (green), and the reactivation of older NW-SE and NE-SW structures, as strike-slip faults (black), all operating under an extensional stress field. Upper Inset: Simplified sketch to show the tectonic model for the Ikaria-Samos Basins developed along strike-slip faulting and oblique rifting: they are bounded by major *en-echelon* arranged faults. The direction of the extension ~N12°E as calculated from the sequence's focal mechanisms (direction of axis σ3, lower inset), in good agreement with the broader stress field (Konstantinou et al., 2017), is oblique to the axis of shearing, clearly depicting the evolution of basins (Samos and Ikaria Basins) within a rather oblique transtensional regime. (For interpretation of the references to colour in this figure legend, the reader is referred to the web version of this article.)

of offshore and onshore sedimentary basins (Philippon et al., 2012; Sakellariou et al., 2013; Beniest et al., 2016). Modern data and modeling (Konstantinou et al., 2017) suggest that the ongoing (back-arc) extension, mainly attributed to the southward trench retreat and slab roll-back, is coupled with shearing. The shearing is imposed from the westward displacement (or escape) of Anatolia along the North Anatolian Fault (Kreemer et al., 2004). This interaction results in a regime where pure normal faulting and pure strike-slip faulting, occasionally combined with strike-slip and dip-slip components, respectively, is observed (Konstantinou et al., 2017). Reflection profiles additionally support a transtensional regime (Sakellariou et al., 2013).

Fig. 7 summarizes how the present-day crustal deformation in the Aegean Sea is accommodated by, or partitioned among, a regional network of faults with different orientations, and how this apparent complexity is depicted by the diversity of earthquake mechanisms (M ≥4.0). Closer to the source of shearing, that is the North Anatolian Fault and its strands entering the Aegean, dextral strike-slip faulting, prevails. The dextral strike-slip motions terminate at the edge of continental Greece. Notably, at the termination of shearing, along NW-SE trending structures, the sense of strike-slip motion is sinistral (Kiratzi, 2002). It is notable also that the strike-slip motions diminish as we move south of ~38° parallel, and normal faulting mainly prevails, as we are closer to the subduction zone, and the effect of trench retreat is more pronounced. This is an observation also noted by the stress inversion results by Konstantinou et al. (2017). More specifically, their results also depict fault diversity, implying stress heterogeneity at the locus of the Samos event (Fig. S6 in their supplement).

Fig. 8, in the context of the above discussion, is a simplified graphic illustration to show how the Samos earthquake contributes to the evolution of two basins (Ikaria and Samos) through active seismic faulting in the modern transtensional tectonic regime. In this model, the basins north of Ikaria and Samos islands, constitute two depocentres, and, due to their proximity, should be jointly examined. The Ikaria Basin is the second deepest (1400 m maximum water depth) basin in the Aegean Sea, after the North Aegean Trough (Sakellariou et al., 2013). Its geometry is rather symmetric and somewhat circular, contrary to the nearby Samos Basin, which is highly asymmetric and considerably shallower (Nomikou et al., 2021). The Samos mainshock is a modern episode of basin evolution through active faulting, as sketched (Fig. 8).

6.3. *The Samos earthquake as another modern signal of localized deformation*

The Samos earthquake adds new evidence of the concentration of the deformation signals along the boundaries of the Aegean plate, as manifested by a cascade of ongoing strong events during the last 15 years or so. Since 2006, 27 strong (M ≥ 6) earthquakes occurred in the Aegean Sea and the surrounding lands (Fig. 9). Most of these events are shallow and have epicenters that remarkably bound the Aegean Plate, while a few occurred within the subducting African lithosphere (depth > 60 km; magenta colors in Fig. 9). Remarkably, all types of deformation are exposed to operate simultaneously, as reflected in the focal mechanisms within this short period: The Africa-Aegean collision, the presence of a subducting plate, the shear motions at the boundaries of the plate, the distributed extension along the overriding plate. In this way, seismology is providing improving constraints for new types of high-resolution

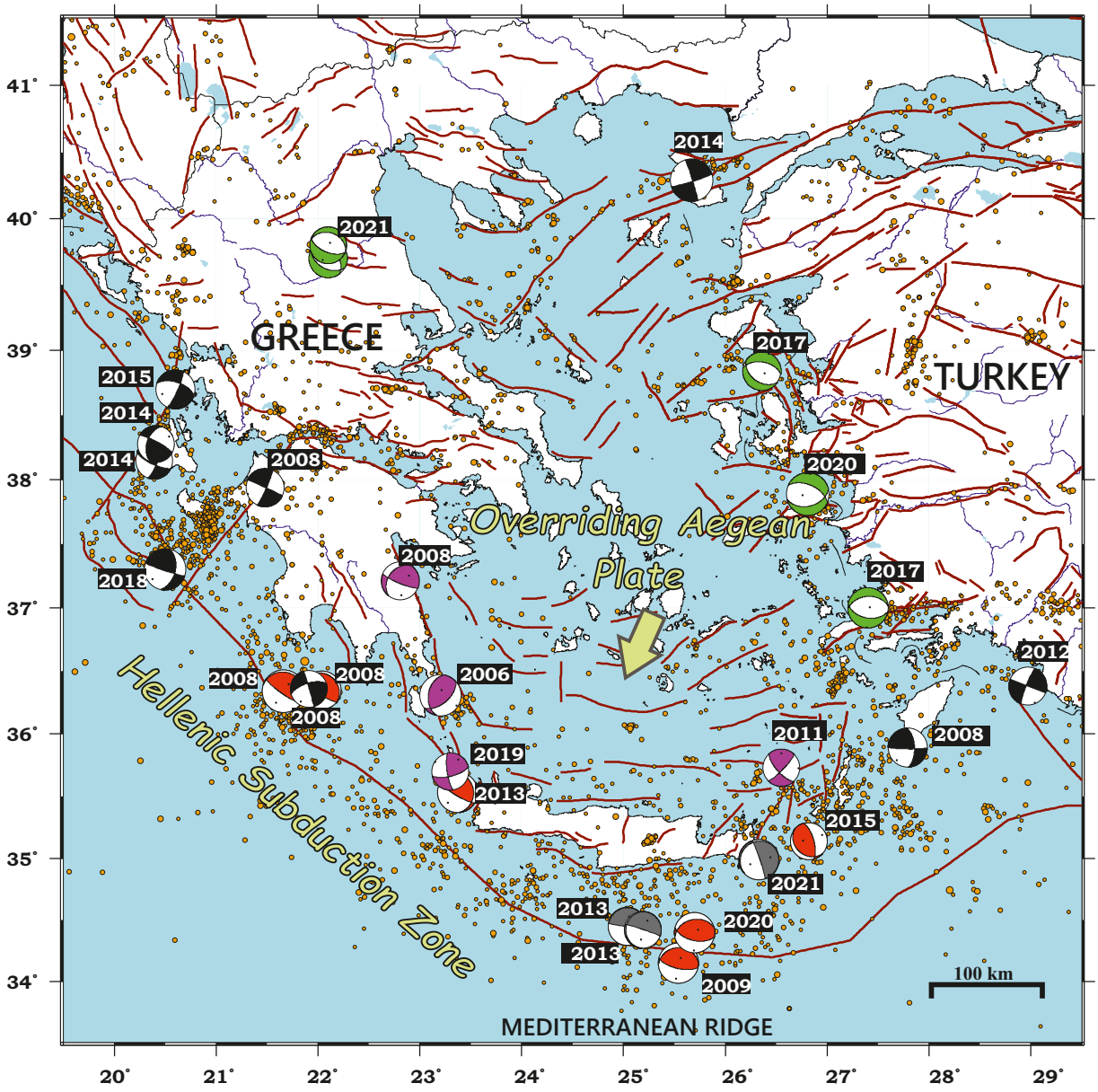

Fig. 9. Localized signals of deformation: Cascade of strong (Mw ≥ 6) earthquakes in the Aegean during the last 15 yr (2006–2021), alongside background seismicity (M > 4; orange circles) for the same period. Magenta beach-balls depict intermediate depth (h > 60 km) events. The remaining ones are shallow, colored red for reverse/thrusts, green for normal faulting, black for strike-slip, and grey for unclassified faulting (three cases near Crete Island). This handful of focal mechanisms depicts all types of deformation of the area: compression along the subduction and within the subducting plate, extension and shear motions along the overriding Aegean plate. (For interpretation of the references to colour in this figure legend, the reader is referred to the web version of this article.)

geodynamic models of the plate interactions.

Within four years (2017 to 2021), the sequential occurrence of normal faulting earthquakes at graben structures, close to coastal western Anatolia events (2017 Lesvos Basin; 2017 Kos-Bodrum Gökova Basin; 2020 Samos Basin) and on the Greek mainland (2021 Thessaly Basin) reflects the intense ~N-S stretching of the upper Aegean Sea plate. Improved seismic networks permitted monitoring of many swarms that occurred along the cross-border region. For example, the swarms in the Gökova basin in 2004 and 2005, the one in Biga Peninsula in 2017, and the currently operating swarm close to the Nisyros volcanic island point to an increased level of localized stresses across the region. This localization and tectonic diversity (complexity) mentioned in the previous paragraph represent a challenge for seismic hazard assessment. Although the Samos earthquake ruptured a known fault, future events nearby may have a different focal mechanism. It calls for a new generation of fault databases including uncertainties.

7. Conclusions

We used broadband and strong-motion waveforms, together with geodetic data, to explore source complexity, finite-fault kinematic modeling, and rupture directivity. We carefully searched for stable features of modeling results by filtering the data at discrete and variable frequency ranges, using all the data and/or selected subsets. Our results confirm the large slip amplitudes (~2.4 m), up-dip and westward rupture propagation, and a near-surface co-seismic slip of ~1 m amplitude, possibly breaking the sea bottom and contributing to observed island uplift and tsunami genesis.

The Samos earthquake expands our view of the effects of the slab back-roll and the southward retreat of the entire subduction system

dominating the Aegean and western Anatolia tectonics. The extension is accommodated by opening parallel-oriented grabens forming basins, such as the Samos-Ikaria basins and Buyuk-Menderes grabens (see Fig. 8). The Samos and Ikaria basins constitute two depocenters that should be jointly examined. The Samos sequence shows the interaction between the long-term evolution of the two basins (formed during the old initiation of dextral transtension in the central Aegean) and active seismic faulting in the transtensional tectonic regime.

As an epilogue, the Samos sequence taught us, in the most dramatic way, that these basins can encompass strong ~Mw7 earthquakes. The hazard imposed on the urban regions across the eastern Aegean Sea was documented. Joint cross-border efforts are needed to better understand the connection and continuation of tectonic structures, especially in the offshore areas, that are less explored.

Data and resources

Digital seismic waveforms were retrieved from the ORFEUS Eida-nodes (https://www.orfeus-eu.org/data/eida/nodes/), and AFAD (https://tadas.afad.gov.tr/event-detail/11995) and catalog and phase data are acquired from the following regional networks: HUSN (HL, doi: https://doi.org/10.7914/SN/HL; HT, doi:https://doi.org/10.7914/SN/HT; HA, doi:https://doi.org/10.7914/SN/HA; HP, doi: https://doi.org/10.7914/SN/HP; HI, doi:https://doi.org/10.7914/SN/HI; HC, doi:https://doi.org/10.7914/SN/HC); KOERI (KO, doi:https://doi.org/10.7914/SN/KO), AFAD (TU, doi.org/10.7914/SN/TU) obtained through the web services of the individual networks and the corresponding EMSC-CSEM online services. Faults were obtained from the Greek Database of Seismogenic Sources (http://gredass.unife.it/GreDaSS_2.0.kmz). The code NonLInLoc used for the mainshock relocations is available at http://alomax.free.fr/nlloc/soft7.00/tar/NLL7.00_src.tgz. The StressInverse code, used in Fig. 8, is available at http://www.ig.cas.cz/en/stress-inverse/. Software ISOLA is available at http://geo.mff.cuni.cz/~jz/for_ISOLAnews/. The Linear Slip Inversion (LinSlipInv) method for kinematic slip inversions can be downloaded from http://fgallovic.github.io/LinSlipInv/. The ASTFs software is available at http://geo.mff.cuni.cz/~vp/ASTFs/. Full reference list of publications related to the Samos earthquake is available from International Seismological Centre, On-line Event Bibliography (http://www.isc.ac.uk/event_bibliography/eventindex.php). Some figures were drawn using the Generic Mapping Tools (GMT) software (Wessel and Smith, 1998). Source time function from SCARDEC Source Time Function database were used for comparison (http://scardec.projects.sismo.ipgp.fr/).

Author contribution

V. Plicka performed mainshock relocation and empirical Green's functions modeling, writing of the original draft.

F. Gallovič performed Linear Slip Inversion, guided the scientific discussion, writing of the original draft.

J. Zahradník performed Multiple point source (MPS) modeling of the mainshock, guided the scientific discussion, writing of the original draft.

A. Serpetsidaki performed relocation of aftershocks, writing of the original draft.

E. Sokos participated in the scientific discussion.

N. Vavlas participated in Linear Slip Inversion.

A. Kiratzi guided the scientific discussion and significantly contributed to seismotectonic interpretation, writing of the original draft.

Declaration of Competing Interest

The authors declare that they have no known competing financial interests or personal relationships that could have appeared to influence the work reported in this paper.

Data availability

All data and information about software availability are described in the Data and Resources section.

Acknowledgments

We acknowledge the duty analysts in Greece and Turkey for the careful analysis of the data, staff members for maintenance and operation of the networks. We also thank our colleague A. Ganas for providing GNSS data before publication. AK and NV acknowledge support by the project "Safe-Schools" which is implemented under the Action "Reinforcement of the Research and Innovation Infrastructure", funded by the Operational Programme "Competitiveness, Entrepreneurship and Innovation" (NSRF 2014-2020) and co-financed by Greece and the EU (European Regional Development Fund). E.S. and A.S acknowledge financial support by the HELPOS project, 'Hellenic Plate Observing System' (MIS 5002697). The authors thank the editor Claire Currie and two anonymous reviewers for their suggestions, which helped us improve this manuscript.

Appendix A. Supplementary data

Supplementary data to this article can be found online at https://doi.org/10.1016/j.tecto.2022.229591.

References

Akyol, N., Zhu, L., Mitchell, B.J., Sözbilir, H., Kekovalı, K., 2006. Crustal structure and local seismicity in western Anatolia. Geophys. J. Int. 166 (3), 1259–1269. https://doi.org/10.1111/j.1365-246X.2006.03053.x.

Beniest, A., Brub, J., Corini, C., Crombez, V., Deschamps, R., Hamon, Y., Smit, J., 2016. Interaction between trench retreat and Anatolian escape as recorded by Neogene basins in the northern Aegean Sea. Mar. Pet. Geol. 77, 30–42. https://doi.org/10.1016/j.marpetgeo.2016.05.011.

Bertero, M., Bindi, D., Boccacci, P., Cattaneo, M., Eva, C., Lanza, V., 1997. Application of the projected Landweber method to the estimation of the source time function in seismology. Inverse Probl. 13, 465–486. https://doi.org/10.1088/0266-5611/13/2/017.

Brun, J.-P., Faccenna, C., Gueydan, F., Sokoutis, D., Philippon, M., Kydonakis, K., Gorini, C., 2016. The two-stage Aegean extension, from localized to distributed, a result of slab rollback acceleration. Can. J. Earth Sci. 53, 1142–1157. https://doi.org/10.1139/cjes-2015-0203.

Calderoni, G., Rovelli, A., Ben-Zion, Y., Di Giovambattista, R., 2015. Along-strike rupture directivity of earthquakes of the 2009 L'Aquila, Central Italy seismic sequence. Geophys. J. Int. 203 (1), 399–415. https://doi.org/10.1093/gji/ggv275.

Caputo, R., Pavlides, S., 2013. The Greek Database of Seismogenic sources (GreDaSS), Version 2.0.0: a compilation of potential seismogenic sources (M>5.5) in the Aegean region. https://doi.org/10.15160/unife/gredass/0200.

Cetin, K., Mylonakis, G., Sextos, A., Stewart, J., Akbaş, B., Akgün, M., et al., 2020. Seismological and Engineering Effects of the M 7.0 Samos Island (Aegean Sea). In: Earthquake. Geotechnical Extreme Events Reconnaissance Association: Report GEER-069. https://doi.org/10.18118/G6H088.

Chatzipetros, A., Kiratzi, A., Sboras, S., Zouros, N., Pavlides, S., 2013. Active faulting in the North-Eastern Aegean Sea Islands. Tectonophysics 597-598, 106–122. https://doi.org/10.1016/j.tecto.2012.11.026.

Chousianitis, K., Konca, A.O., 2021. Rupture process of the 2020 Mw7.0 Samos earthquake and its effect on surrounding active faults. Geophys. Res. Lett. 48 https://doi.org/10.1029/2021GL094162 e2021GL094162.

Courboulex, F., Santoyo, M.A., Pacheco, J.F., Singh, S.K., 1997. The September 14 1995 (M = 7.3) Copala, Mexico, earthquake: a source study using teleseismic, regional, and local data. Bull. Seismol. Soc. Am. 87 (4), 999–1010.

Dogan, G.G., Yalciner, A.C., Yuksel, Y., Ulutaş, E., Polat, O., Güler, I., Şahin, C., Tarih, A., Kânoğlu, U., 2021. The 30 October 2020 Aegean Sea Tsunami: Post-Event Field Survey along Turkish Coast. Pure Appl. Geophys. 178, 785–812. https://doi.org/10.1007/s00024-021-02693-3.

Dziewonski, A.M., Chou, T.-A.T., Woodhouse, J.H., 1981. Determination of earthquake source parameters from waveform data for studies of global and regional seismicity. J. Geophys. Res. 86, 2825–2852. https://doi.org/10.1029/JB086iB04p02825.

Ekström, G., Nettles, M., Dziewoński, A.M., 2012. The global CMT project 2004-2010: centroid-moment tensors for 13,017 earthquakes. Phys. Earth Planet. Inter. 200–201, 1–9. https://doi.org/10.1016/j.pepi.2012.04.002.

England, P., Houseman, G., Nocquet, J.-M., 2016. Constraints from GPS measurements on the dynamics of deformation in Anatolia and the Aegean. J. Geophys. Res. Solid Earth 121 (12), 8888–8916. https://doi.org/10.1002/2016JB013382.

Evelpidou, N., Karkani, A., Kampolis, I., 2021. Relative sea level changes and morphotectonic implications triggered by the Samos earthquake of October 30 2020. J. Mar. Sci. Eng. 9.
Faccenna, C., Becker, T.W., Auer, L., Billi, A., Boschi, L., Brun, J.P., Capitanio, F.A., Funiciello, F., Horvàth, F., Jolivet, L., Piromallo, C., Royden, L., Rossetti, F., Serpelloni, E., 2014. Mantle dynamics in the Mediterranean. Rev. Geophys. 52 (3), 283–332. https://doi.org/10.1002/2013RG000444.
Foumelis, M., Papazachos, C., Papadimitriou, E., Karakostas, V., Ampatzidis, D., Moschopoulos, G., Kostoglou, A., Ilieva, M., Minos-Minopoulos, D., Mouratidis, A., Kkallas, Ch., Chatzipetros, A., 2021. On rapid multidisciplinary response aspects for Samos 2020 M7.0 earthquake. Acta Geophysica 69, 1025–1048. https://doi.org/10.1007/s11600-021-00578-6.
Gallovič, F., 2016. Modeling Velocity Recordings of the Mw 6.0 South Napa, California, earthquake: Unilateral Event with Weak High-Frequency Directivity. Seismol. Res. Lett. 87 (1), 2–14. https://doi.org/10.1785/0220150042.
Gallovič, F., Zahradník, J., 2011. Toward understanding slip-inversion uncertainty and artifacts II: singular value analysis. J. Geophys. Res. 116, B02309.
Gallovič, F., Imperatori, W., Mai, P.M., 2015. Effects of three-dimensional crustal structure and smoothing constraint on earthquake slip inversions: Case study of the Mw6.3 2009 L'Aquila earthquake. J. Geophys. Res. Solid Earth 120 (1), 428–449. https://doi.org/10.1002/2014JB011650.
Gallovič, F., Valentová, Ľ., Ampuero, J.-P., Gabriel, A.-A., 2019. Bayesian Dynamic Finite-Fault Inversion: 2. Application to the 2016 Mw6.2 Amatrice, Italy, Earthquake. J. Geophys. Res. Solid Earth 124, 6970–6988.
Ganas, A., Elias, P., Briole, P., Tsironi, V., Valkaniotis, S., Escartin, J., Karasante, I., Efstathiou, E., 2020. Fault responsible for Samos earthquake identified. Temblor. https://doi.org/10.32858/temblor.134.
Ganas, A., Elias, P., Briole, P., Valkaniotis, S., Escartin, J., Tsironi, V., Karasante, I., Kosma, C., 2021. Co-seismic and postseismic deformation, field observations and fault model of the October 30, 2020 Mw=7.0 Samos earthquake, Aegean Sea. Acta Geophysica 69, 999–1024. https://doi.org/10.1007/s11600-021-00599-1.
Hartzell, S.H., 1978. Earthquake aftershocks as Green's functions. Geophys. Res. Lett. 5, 1–4. https://doi.org/10.1029/GL005i001p00001.
Jolivet, L., Menant, A., Sternai, P., Rabillard, A., Arbaret, L., Augier, R., Laurent, V., Beaudoin, A., Grasemann, B., Huet, B., Labrousse, L., le Pourhiet, Laetitia, 2015. The geological signature of a slab tear below the Aegean. Tectonophysics 659. https://doi.org/10.1016/j.tecto.2015.08.004.
Karabulut, H., Paul, A., Özbakır, A.D., Ergün, T., Şentürk, S., 2019. A new crustal model of the Anatolia–Aegean domain: evidence for the dominant role of isostasy in the support of the Anatolian plateau. Geophys. J. Int. 218 (1), 57–73. https://doi.org/10.1093/gji/ggz147.
Karakostas, V., Tan, O., Kostoglou, A., Papadimitriou, E., Bonatis, P., 2021. Seismotectonic implications of the 2020 Samos, Greece, Mw 7.0 mainshock based on high-resolution aftershock relocation and source slip model. ActaGeophysica 69, 979–996. https://doi.org/10.1007/s11600-021-00580-y.
Kiratzi, A., 2002. Stress tensor inversions along the westernmost North Anatolian Fault Zone and its continuation into the North Aegean Sea. Geophys. J. Int. 151 (2), 360–376.
Kiratzi, A., Koskosidi, A., 2018. Constrains on the near-source motions of the Kos-Bodrum 20 July 2017 Mw6.6 earthquake. In: Proceedings: 16th European Conference on Earthquake Engineering, Thessaloniki, Greece, p. 13 (ID 11450).
Kiratzi, A., Papazachos, C., Özacar, A., Pinar, A., Kkallas, Ch., Sopachi, E., 2021. Characteristics of the 2020 Samos earthquake (Aegean Sea) using seismic data. Bull. Earthq. Eng. https://doi.org/10.1007/s10518-021-01239-1.
Konca, A.O., Guvercin, S.E., Ozarpaci, S., Ozdemir, A., Funning, G.J., Dogan, U., Ergintav, S., Floyd, M., Karabulut, H., Reilinger, R., 2019. Slip distribution of the 2017 Mw6.6 Bodrum–Kos earthquake: resolving the ambiguity of fault geometry. Geophys. J. Int. 219 (2), 911–923.
Konstantinou, K.I., 2018. Estimation of optimum velocity model and precise earthquake locations in NE Aegean: Implications for seismotectonics and seismic hazard. J. Geodyn. 121, 143–154. https://doi.org/10.1016/j.jog.2018.07.005.
Konstantinou, K.I., Mouslopoulou, V., Liang, W.-T., Heidbach, O., Oncken, O., Suppe, J., 2017. Present-day crustal stress field in Greece inferred from regional-scale damped inversion of earthquake focal mechanisms. J. Geophys. Res. Solid Earth 122, 506–523. https://doi.org/10.1002/2016JB013272.
Kreemer, C., Chamot-Rooke, N., Le Pichon, X., 2004. Constraints on the evolution and vertical coherency of deformation in the Northern Aegean from a comparison of geodetic, geologic and seismologic data. Earth Planet. Sci. Lett. 225, 329–346. https://doi.org/10.1016/j.epsl.2004.06.018.
Laigle, M., Hirn, A., Sachpazi, M., Rousos, N., 2000. North Aegean crustal deformation: An active fault imaged to 10 km depth by reflection seismic data. Geology 28, 71–74.
Laske, G., Masters, G., Ma, Z., Pasyanos, M., 2013. Update on CRUST1.0 – A 1-degree Global Model of Earth's Crust. In: EGU General Assembly Conference Abstracts (pp. EGU2013-2658).
Lawson, C.L., Hanson, R.J., 1974. Solving least squares problems. In: Prentice-Hall Series in Automatic Computation.
Le Pichon, X., Şengör, A.C., İmren, C., 2019. A new approach to the opening of the eastern Mediterranean Sea and the origin of the Hellenic Subduction Zone. Part 1: the eastern Mediterranean Sea. Can. J. Earth Sci. 56, 1119–1143.
Lentas, K., Gkarlaouni, C.G., Kalligeris, N., Melis, N.S., 2021. The October 30 2020, MW = 7.0, Samos earthquake: aftershock relocation, slip model, Coulomb stress evolution and estimation of shaking. Bull. Earthq. Eng. https://doi.org/10.1007/s10518-021-01260-4.
Liu, J., Zahradník, J., 2020. The 2019 MW 5.7 Changning earthquake, Sichuan Basin, China: a shallow doublet with different faulting styles. Geophys. Res. Lett. 47 https://doi.org/10.1029/2019GL085408 e2019GL085408.
Lomax, A., Virieux, J., Volant, P., Berge-Thierry, C., 2000. Probabilistic Earthquake Location in 3D and Layered Models. In: Thurber, C.H., Rabinowitz, N. (Eds.), Advances in Seismic Event Location. Springer Netherlands, Dordrecht, pp. 101–134. https://doi.org/10.1007/978-94-015-9536-0_5.
López-Comino, J.A., Cesca, S., 2018. Source complexity of an injection induced event: the 2016 Mw 5.1 Fairview, Oklahoma earthquake. Geophys. Res. Lett. 45, 4025–4032. https://doi.org/10.1029/2018GL077631.
Makra, K., Rovithis, E., Riga, E., Raptakis, D., Pitilakis, K., 2021. Amplification features and observed damages in İzmir (Turkey) due to 2020 Samos (Aegean Sea) earthquake: identifying basin effects and design requirements. Bull. Earthq. Eng. 19 (12), 4773–4804.
McGuire, J.J., 2004. Estimating finite source properties of small earthquake ruptures. Bull. Seismol. Soc. Am. 94, 377–393. https://doi.org/10.1785/0120030091.
Meng, J., Sinoplu, O., Zhou, Z., Tokay, B., Kusky, T., Bozkurt, E., Wang, L., 2021. Greece and Turkey shaken by African tectonic retreat. Sci. Rep. 11 (1), 6486. https://doi.org/10.1038/s41598-021-86063-y.
Mori, J., Hartzell, S., 1990. Source inversion of the 1988 Upland, California, earthquake: Determination of a fault plane for a small event. Bull. Seismol. Soc. Am. 80, 507–518.
Mueller, C.S., 1985. Source pulse enhancement by deconvolution of an empirical Green's function. Geophys. Res. Lett. 12, 33–36. https://doi.org/10.1029/GL012i001p00033.
Nomikou, P., Evangelidis, D., Papanikolaou, D., Lampridou, D., Litsas, D., Tsaparas, Y., Koliopanos, I., 2021. Morphotectonic Analysis along the Northern margin of Samos Island, Related to the Seismic activity of October 2020, Aegean Sea, Greece. Geosciences 11 (2). https://doi.org/10.3390/geosciences11020102.
Novotný, O., Zahradník, J., Tselentis, G.-A., 2001. Northwestern Turkey Earthquakes and the Crustal Structure Inferred from Surface Waves Observed in Western Greece. Bull. Seismol. Soc. Am. 91 (4), 875–879. https://doi.org/10.1785/0120000116.
Özer, Ç., Polat, O., 2017. 3-D crustal velocity structure of Izmir and surroundings. J. Fac. Eng. Archit. Gazi Univ. 32 (3), 733–747.
Özer, Ç., Gök, E., Polat, O., 2018. Three-Dimensional Seismic Velocity Structure of the Aegean Region of Turkey from local Earthquake Tomography. Ann. Geophys. 61 https://doi.org/10.4401/ag-7543.
Pacor, F., Gallovič, F., Puglia, R., Luzi, L., D'Amico, M., 2016. Diminishing high-frequency directivity due to a source effect: empirical evidence from small earthquakes in the Abruzzo region, Italy. Geophys. Res. Lett. 43, 5000–5008.
Papadimitriou, P., Kapetanidis, V., Karakonstantis, A., Spingos, I., Kassaras, I., Sakkas, V., Kouskouna, V., Karatzetzou, A., Pavlou, K., Kaviris, G., Voulgaris, N., 2020. First results on the Mw=6.9 Samos earthquake of October 30 2020. Bull. Geol. Soc. Greece 56, 251–279.
Philippon, M., Brun, J.-P., Gueydanc, F., 2012. Deciphering subduction from exhumation in the segmented Cycladic Blueschist Unit (Central Aegean, Greece). Tectonophysics 524-525, 116–134. https://doi.org/10.1016/j.tecto.2011.12.025.
Pizzi, A., Di Domenica, A., Gallovič, F., Luzi, L., Puglia, R., 2017. Fault segmentation as constraint to the occurrence of the main shocks of the 2016 Central Italy seismic sequence. Tectonics 36, 2370–2387.
Ren, Ch., Yue, H., Cao, B., Zhu, Y., Wang, T., An, Ch., Ge, Z., Li, Z., 2022. Rupture process of the 2020 Mw = 6.9 Samos, Greece earthquake on a segmented fault system constrained from seismic, geodetic, and tsunami observations. Tectonophysics 839, 229497. https://doi.org/10.1016/j.tecto.2022.229497.
Roumelioti, Z., Benetatos, C., Kiratzi, A., 2009. The February 14 2008 earthquake (M6.7) sequence offshore South Peloponnese (Greece): source models of the three strongest events. Tectonophysics 471, 272–284. https://doi.org/10.1016/j.tecto.2009.02.028.
Sakellariou, D., Mascle, J., Lykousis, V., 2013. Strike slip tectonics and transtensional deformation in the Aegean region and the Hellenic arc: preliminary results. Bull. Geol. Soc. Greece 47. https://doi.org/10.12681/bgsg.11098.
Sokos, E., Kiratzi, A., Gallovič, F., Zahradník, J., Serpetsidaki, A., Plicka, V., Janský, J., Kostelecký, J., Tselentis, G.-A., 2015. Rupture process of the 2014 Cephalonia, Greece, earthquake doublet (Mw6) as inferred from regional and local seismic data. Tectonophysics 656, 131–141.
Sokos, E., Zahradník, J., Gallovič, F., Serpetsidaki, A., Plicka, V., Kiratzi, A., 2016. Asperity break after 12 years: the Mw6.4 2015 Lefkada (Greece) earthquake. Geophys. Res. Lett. 43, 6137–6145.
Sokos, E., Gallovič, F., Evangelidis, C.P., Serpetsidaki, A., Plicka, V., Kostelecký, J., Zahradník, J., 2020. The 2018 Mw 6.8 Zakynthos, Greece, earthquake: Dominant Strike-Slip Faulting near Subducting Slab. Seismol. Res. Lett. 91 (2A), 721–732. https://doi.org/10.1785/0220190169.
Taymaz, T., Yolsal-Çevikbilen, S., Irmak, T.S., Vera, F., Liu, Ch., Eken, T., Zhang, Z., Erman, C., Keleş, D., 2022. Kinematics of the 30 October 2020 Mw 7.0 Néon Karlovásion (Samos) earthquake in the Eastern Aegean Sea: Implications on source characteristics and dynamic rupture simulations. j 229223. https://doi.org/10.1016/j.tecto.2022.229223.
Triantafyllou, I., Gogou, M., Mavroulis, S., Lekkas, E., Papadopoulos, G.A., Thravalos, M., 2021. The Tsunami Caused by the October 30 2020 Samos (Aegean Sea) Mw7.0 earthquake: Hydrodynamic Features, Source Properties and Impact Assessment from Post-Event Field Survey and Video Records. J. Mar. Sci. Eng. 9, 68. https://doi.org/10.3390/jmse9010068.
Vallée, M., 2004. Stabilizing the empirical Green function analysis: Development and the projected Landweber method. Bull. Seismol. Soc. Am. 94, 394–409. https://doi.org/10.1785/0120030017.
Vallée, M., Douet, V., 2016. A new database of Source Time Functions (STFs) extracted from the SCARDEC method. Phys. Earth Planet. Inter. 257, 149–157.
Vallée, M., Charléty, J., Ferreira, A.M.G., Delouis, B., Vergoz, J., 2011. SCARDEC: a new technique for the rapid determination of seismic moment magnitude, focal mechanism and source time functions for large earthquakes using body-wave

deconvolution. Geophys. J. Int. 184 (1), 338–358. https://doi.org/10.1111/j.1365-246X.2010.04836.x.
Waldhauser, F., 2001. hypoDD—A program to compute double-difference hypocenter locations. Open-File Report. https://doi.org/10.3133/ofr01113.
Waldhauser, F., Ellsworth, W.L., 2000. A Double-difference Earthquake location algorithm: Method and application to the Northern Hayward Fault, California. Bull. Seismol. Soc. Am. 90 (6), 1353–1368. https://doi.org/10.1785/0120000006.
Weiss, J.R., Walters, R.J., Morishita, Y., Wright, T.J., Lazecky, M., Wang, H., et al., 2020. High-resolution surface velocities and strain for Anatolia from Sentinel-1 InSAR and GNSS data. Geophys. Res. Lett. 47 https://doi.org/10.1029/2020GL087376 e2020GL087376.
Wessel, P., Smith, W.H.F., 1998. New, improved version of generic mapping tools released. EOS Trans. Am. Geophys. Union 79 (47), 579. https://doi.org/10.1029/98EO00426.
Zahradník, J., Gallovič, F., 2010. Toward understanding slip-inversion uncertainty and artifacts. J. Geophys. Res. 115, B09310.
Zahradník, J., Sokos, E., 2014. The M w 7.1 Van, Eastern Turkey, earthquake 2011: two-point source modelling by iterative deconvolution and non-negative least squares. Geophys. J. Int. 196 (1), 522–538.
Zahradník, J., Sokos, E., 2018. ISOLA Code for Multiple-Point Source Modeling—Review. In: D'Amico, S. (Ed.), Moment Tensor Solutions: A Useful Tool for Seismotectonics. Springer International Publishing, Cham, pp. 1–28. https://doi.org/10.1007/978-3-319-77359-9_1.
Zúñiga, F.R., Tan, O., 2021. Introduction to the special issue on the October 30, 2020, Mw7.0, Samos Island, Greece, earthquake. Acta Geophysica 69, 975–977. https://doi.org/10.1007/s11600-021-00612-7.